

Supplementary Information

Fe–N-doped carbon-based composite as an efficient and durable electrocatalyst for the oxygen reduction reaction

Gasidit Panomsuwan,^{*ab} Nagahiro Saito,^{bcd} and Takahiro Ishizaki^{*de}

^a Department of Materials Engineering, Faculty of Engineering, Kasetsart University, Bangkok 10900, Thailand

^b NU-PPC Plasma Chemical Technology Laboratory, The Petroleum and Petrochemical College, Chulalongkorn University, Bangkok 10330, Thailand

^c Department of Materials, Physics and Energy Engineering, Graduate School of Engineering, Nagoya University, Nagoya 464-8603, Japan

^d Core Research for Evolutional Science and Technology (CREST), Japan Science and Technology Agency (JST), Saitama 332-0012, Japan

^e Department of Materials Science and Engineering, Faculty of Engineering, Shibaura Institute of Technology, Tokyo 135-8548, Japan

*Corresponding authors: g.panomsuwan@gmail.com; ishizaki@sic.shibaura-it.ac.jp

Experimental section

Materials

Ethanol (C_2H_5OH , $\geq 99.5\%$ purity), methanol (CH_3OH , $\geq 99.5\%$ purity), concentrated hydrochloric acid (HCl, 35.0–37.0%), and 0.1 M potassium hydroxide aqueous solution (0.1 M KOH, $\geq 99.5\%$ purity) were purchased from Kanto Chemical Co., Inc. Ferrocene ($Fe(C_2H_5)_2$, $> 98.0\%$ purity) was purchased from Wako Pure Chemical Industries Ltd. 2-Cyanopyridine ($C_6H_4N_2$, $\geq 99.0\%$ purity), Nafion® DE 521 solution (5 wt % in a mixture of lower aliphatic alcohols and water), and 20 wt % Pt on Vulcan XC-72 (20% Pt/C) were purchased from Sigma Aldrich. Ultrapure water (18.2 M Ω cm at 25 °C) was obtained by purification with an Advantec RFD 250 NB system. All chemicals were of analytical grade and used without further purification.

Synthesis of CNF

The CNFs were prepared by a floating reactant method following the procedure reported by Endo et al.^[S1] Briefly, ferrocene and hydrogen sulfide were both used as the catalyst precursor, while natural gas was used as a carbon feedstock in the synthesis. Graphitization of the CNF was performed at 3000 °C for 10 min under a high-purity Ar atmosphere in a graphite-resistant furnace. The resulting CNFs were subsequently treated by HCl solution at 80 °C for 6 h to remove the residual Fe catalysts.

Synthesis of Fe–N–CNP–CNF composite

100 mg of CNFs were added in 100 mL of 2-cyanopyridine under vigorous stirring and sonication for 30 min each to obtain a homogeneous suspension. The homogeneous suspension was then poured into a glass reactor, in which a symmetric pair of 1-mm diameter Fe electrode (99.5% purity, The Nilaco Corporation) shielded with an insulating ceramic tube was placed at the center with an initial gap distance of 1.0 mm (Fig. S1). A bipolar pulsed voltage of about 1.5–2.0 kV was applied to the Fe electrodes using an MPP-HV04 Pekuris power generator (Kurita Seisakusho Co., Ltd.). The pulse duration and repetition frequency were fixed at 0.80 μ s and 20 kHz, respectively, to obtain stable and continuous plasma throughout the synthesis. Plasma was generated and stably maintained inside the suspension under vigorous stirring for 30 min. The resulting Fe–N–CNP–CNF composite was separated by filtration and repeatedly washed with ethanol until the wash solvent was colorless. The Fe–N–CNP–CNF composite was then dried at 60 °C for 12 h under ambient conditions and ground with an agate mortar and pestle. Finally, the Fe–N–CNP–CNF composite was loaded into a ceramic boat and then subsequently transferred into a quartz tube placed inside a tubular furnace. The heat treatment was performed at 900 °C for 1 h with a heating rate of 5 °C min⁻¹ under an Ar flow rate of 500 mL min⁻¹ and cooled naturally to room temperature under the same environment. For comparison, N–CNP–CNF and N–CNP were also synthesized from 2-cyanopyridine under the same conditions with use of tungsten as the electrodes.

Characterizations

Field-emission scanning electron microscopy (FESEM) images were taken on a Hitachi S-4800 microscope operated at an accelerating voltage of 10 kV. Transmission electron microscopy (TEM) images, high-resolution TEM (HRTEM) images, and selected area electron diffraction (SAED) patterns were acquired using a JEOL JEM-2100 microscope operated at an accelerating voltage of 120 kV. Elemental mapping images were taken with a JEOL JEM-2500SE microscope operated at an accelerating voltage of 200 kV. N_2 adsorption–desorption isotherms were measured on a Belsorp-mini II sorption analyzer at liquid N_2 temperature ($-196\text{ }^\circ\text{C}$) to investigate specific surface area, pore volume, and pore size distribution of the catalysts. Prior to the measurement, all catalysts were heated at $150\text{ }^\circ\text{C}$ for 90 min under vacuum. The specific surface area was determined by the Brunauer–Emmett–Teller (BET) method at relative pressures (P/P_0) between 0.05 and 0.30. The pore volume and pore-size distribution were determined by the Barrett–Joyner–Halenda (BJH) method. X-ray diffraction (XRD) patterns were recorded on a Rigaku Ultima IV diffractometer with $\text{Cu K}\alpha$ radiation ($\lambda = 0.15406\text{ nm}$) at 40 kV and 40 mA. Raman spectra were recorded on a JASCO NRS-5100 spectrometer with a laser-excitation wavelength of 532.1 nm. X-ray photoelectron spectroscopy (XPS) measurements were carried out on a JEOL JPS-9010MC spectrometer with monochromatic $\text{Mg K}\alpha$ radiation (1253.6 eV) as an X-ray source. The emission current and anode voltage were operated at 25 mA and 10 kV, respectively.

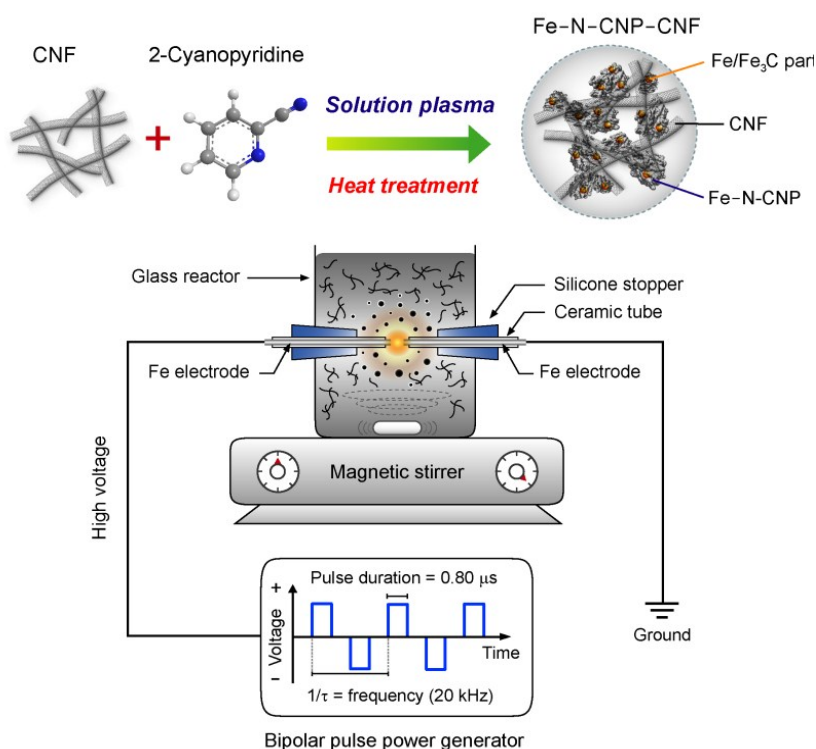


Fig. S1 Schematic representation of the solution plasma process system used for the preparation of Fe-N-CNP-CNF.

Optical emission spectroscopy measurement

Optical emission spectrum of the plasma generated inside 2-cyanopyridine without the dispersion of CNFs was recorded with an Avantes AvaSpec-3648 fiber optic spectrometer system in the wavelengths from 300 to 800 nm. The spectrum was recorded by averaging 3 scans with a 200-ms integration time. The optical probe was set at about 15 mm above the plasma zone.

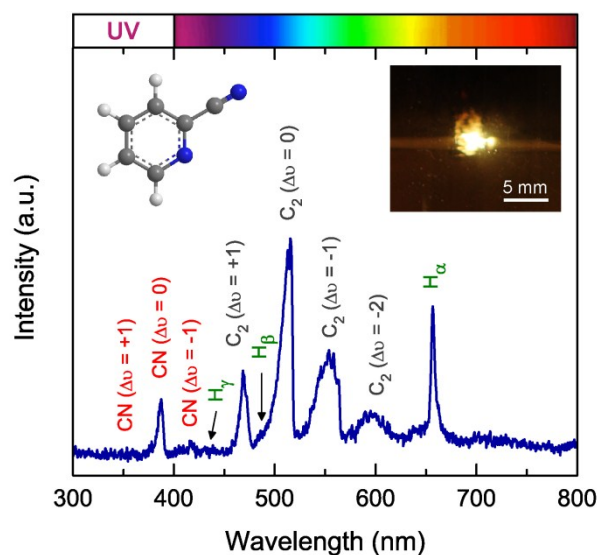


Fig. S2 Optical emission spectrum of the plasma generated in 2-cyanopyridine without CNFs. The optical emission spectrum shows the dominant emissions of Swan bands originating from diatomic carbon (C_2) (transition $d^3\Pi_g \rightarrow a^3\Pi_u$; sequences $\Delta v = -2, -1, 0, +1, +2$) at the wavelength range of 432–630 nm.^[S2] The emission peaks at 434, 487, and 656 nm are associated with Balmer atomic hydrogen H_γ , H_β , and H_α , respectively.^[S3] The emission peaks corresponding to the CN radicals (transition $B^2\Sigma^+ \rightarrow X^2\Sigma^+$ sequence $\Delta v = -1, 0, +1$) are also observed at the shorter wavelengths of 350–420 nm.^[S4,S5]

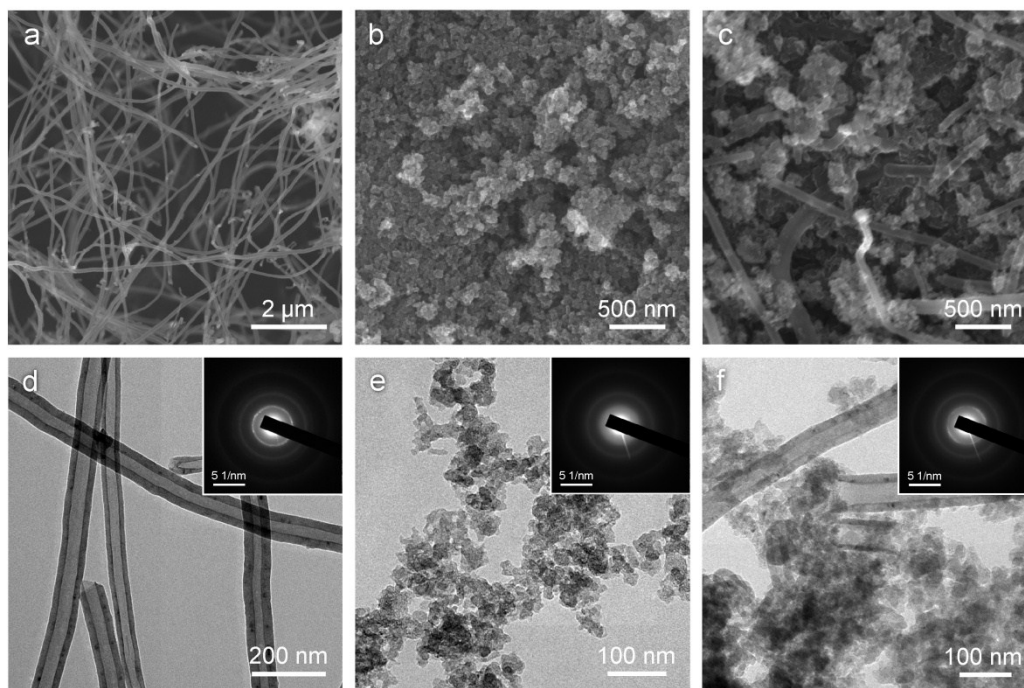


Fig. S3 FE-SEM images of (a) CNF, (b) N-CNP, and (c) N-CNP–CNF. TEM images of (d) CNF, (e) N-CNP, and (f) N-CNP–CNF. The SAED patterns are shown in the inset of their corresponding TEM images.

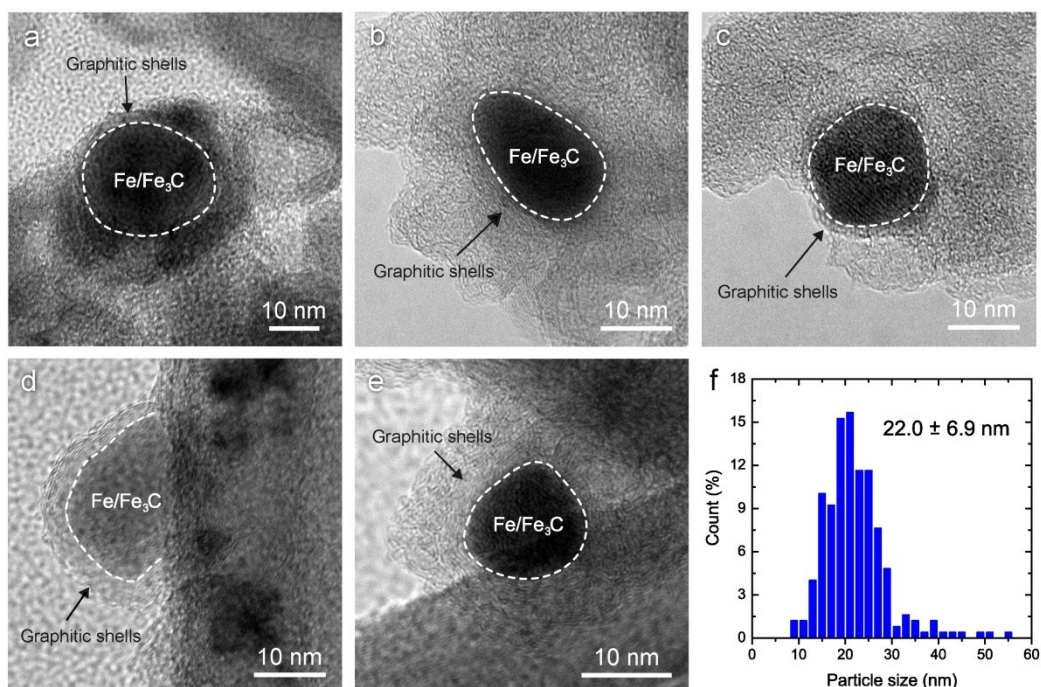


Fig. S4 (a–e) HRTEM images at the area of individual Fe/Fe₃C particle encapsulated in graphitic shells. (f) Size distribution of Fe/Fe₃C particles deduced from 500 particles.

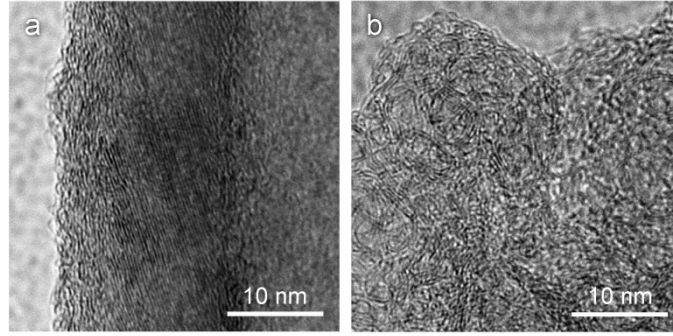


Fig. S5 HR-TEM images of Fe-N-CNP-CNF at the areas where the CNF (a) and (b) N-CNP exist.

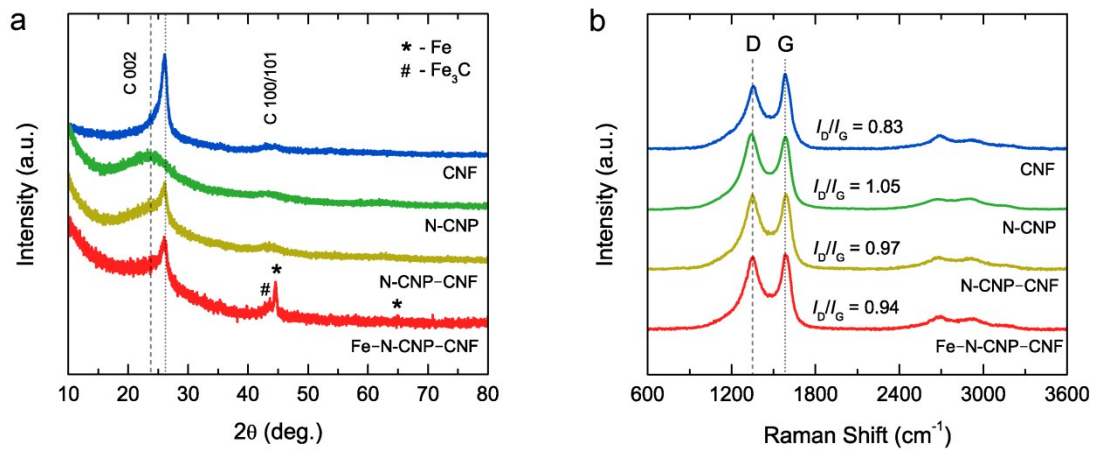


Fig. S6 (a) XRD and (b) Raman spectra of CNF, N-CNP, N-CNP-CNF, and Fe-N-CNP-CNF.

Table S1 Textural parameters of CNF, N-CNP, N-CNP–CNF, and Fe–N-CNP–CNF obtained from the N₂ adsorption–desorption isotherms

	Specific surface area (m ² g ⁻¹)	Pore volume (cm ³ g ⁻¹)	Mean pore size (nm)
CNF	42.40	0.24	25.55
N-CNP	171.91	0.94	39.01
N-CNP–CNF	159.76	0.80	53.04
Fe–N-CNP–CNF	156.54	0.74	28.65

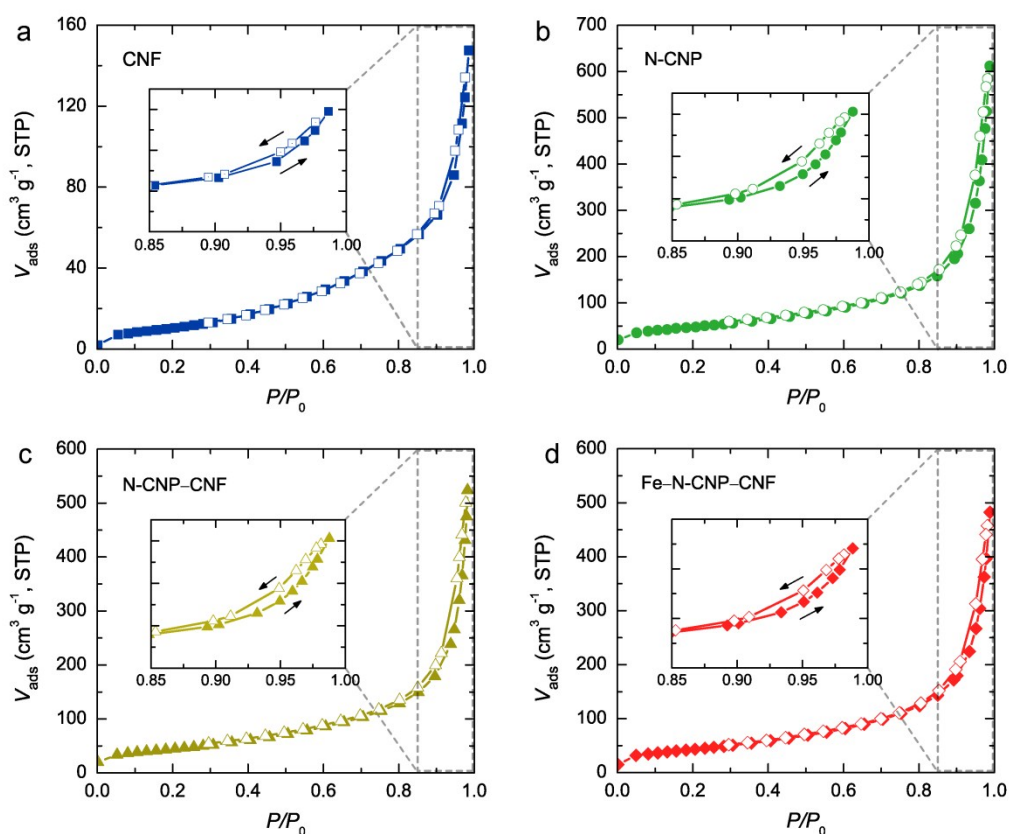


Fig. S7 N₂ adsorption–desorption isotherms of (a) CNF, (b) N-CNP, (c) N-CNP–CNF, and (d) Fe–N-CNP–CNF. The inset of each figure shows the enlarged N₂ adsorption–desorption isotherms at the relative pressure region of 0.85–1.0 where the narrow hysteresis loop was observed for N-CNP, N-CNP–CNF, and Fe–N-CNP–CNF

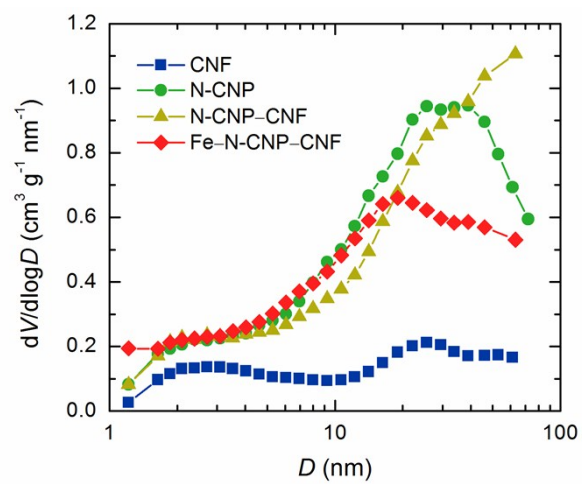


Fig. S8 Pore-size distribution determined from the BJH method of CNF, N-CNP, N-CNP–CNF, and Fe–N-CNP–CNF.

Table S2 Surface elemental compositions of CNF, N-CNP, N-CNP–CNF, Fe–N-CNP–CNF obtained from the XPS quantitative analysis.

	Surface elemental composition (at%)			
	C	O	N	Fe
CNF	91.63	8.37	-	-
N-CNP	91.69	6.98	1.33	-
N-CNP–CNF	91.87	6.78	1.35	-
Fe–N-CNP–CNF	90.10	8.59	1.16	0.15

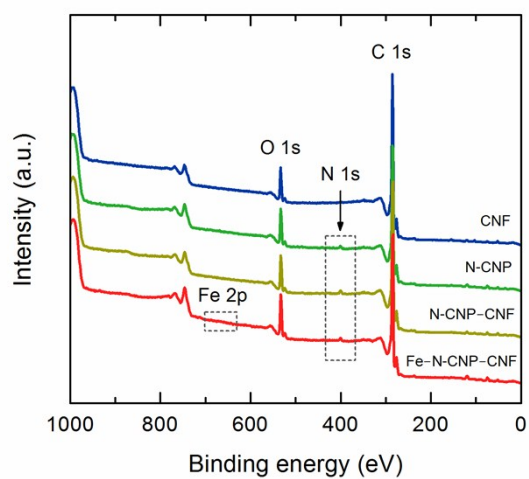


Fig. S9 XPS survey spectra of CNF, N-CNP, N-CNP–CNF, and Fe–N-CNP–CNF.

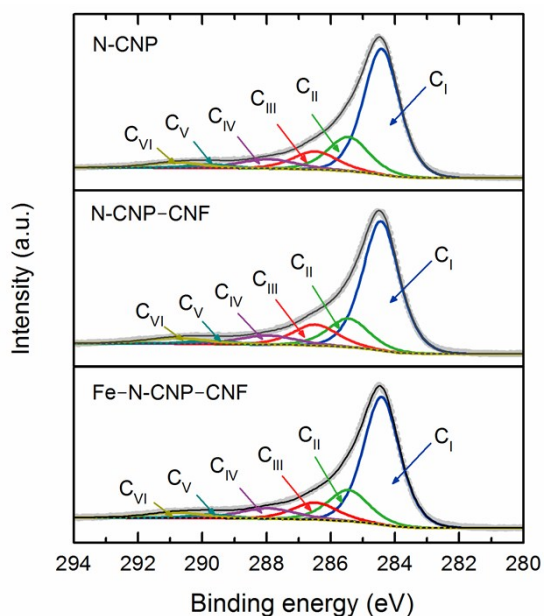


Fig. S10 High-resolution XPS C 1s spectra of N-CNP, N-CNP–CNF, and Fe–N-CNP–CNF. The XPS C 1s peak can be deconvoluted into six peaks. The most pronounced peak at 284.5 eV (C_I) is evidence that the carbons are present in the sp^2 graphite structural form. The other five peaks at the tail of asymmetric XPS C 1s peak can be assigned to the presence of sp^3 bond (C_{II} : 285.4 eV), C–O/C=N (C_{III} : 286.4 eV), C=O/C–N (C_{IV} : 288.0 eV), C=O bonds of different types (carbonyl, aldehyde, etc.) (C_V : 289.2 eV), and π – π interactions (C_{VI} : 290.8 eV).

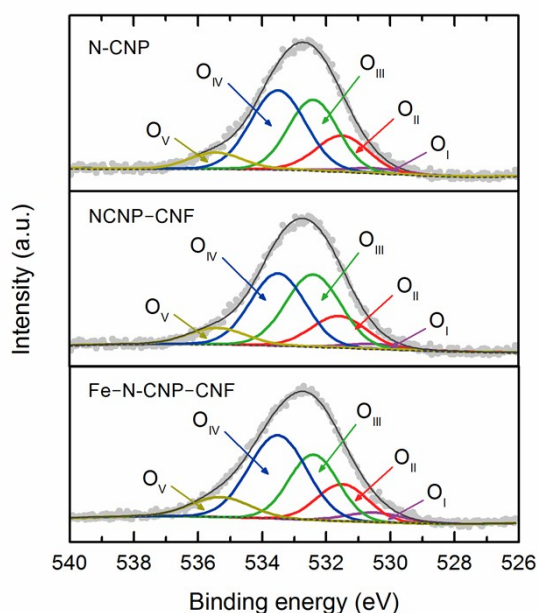


Fig. S11 High-resolution XPS O 1s spectra of N-CNP, N-CNP–CNF, and Fe–N-CNP–CNF. The XPS O 1s peak can be deconvoluted into five peaks, including quinines (O_I : 530.5 eV), C=O (O_{II} : carbonyl and carboxyl; 531.5 eV), C–O (O_{III} : epoxy and hydroxyl, 532.4 eV), OH (O_{IV} : hydroxyl, 533.5 eV), and adsorbed molecular water (O_V , 535.5 eV).

Table S3 Relative percentages and absolute contents of various nitrogen states for N-CNP, N-CNP–CNF, and Fe–N-CNP–CNF obtained from the deconvolution of XPS N 1s peaks

	Relative percentage (%) / Absolute content (at%)			
	Pyridinic N	Pyrrolic N	Graphitic N	Pyridinic N-oxide
N-CNP	20.5 / 0.27	-	67.8 / 0.90	11.7 / 0.16
N-CNP–CNF	25.1 / 0.34	-	64.3 / 0.87	10.6 / 0.14
Fe–N-CNP–CNF	19.8 / 0.23	-	73.0 / 0.85	7.2 / 0.08

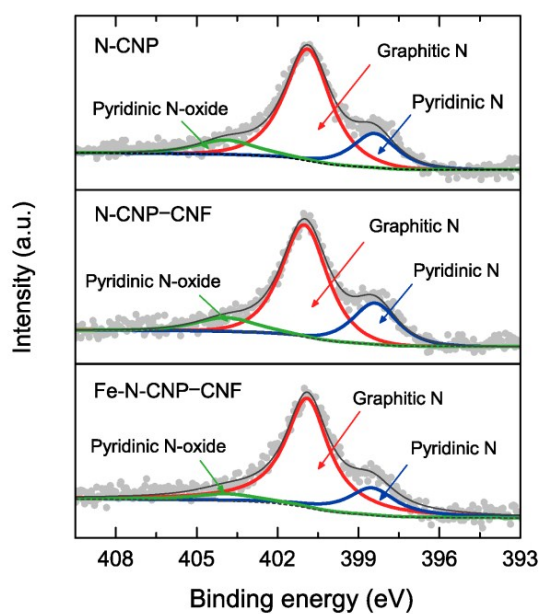


Fig. S12 High-resolution XPS N 1s spectra of N-CNP, N-CNP–CNF, and Fe–N-CNP–CNF. The spectra can be deconvoluted into three peaks, including pyridinic N (N1: 398.4 ± 0.1 eV), graphitic N (N2: 400.9 ± 0.1 eV), and pyridinic N-oxide (N3: 403.5 ± 0.2 eV).

Electrochemical measurements

A glassy carbon electrode was polished on the polishing pad with a 0.1 μm diamond slurry and 0.05 μm alumina slurry in a figure-eight pattern for 2 min each to obtain a mirror surface, respectively. The polished electrode was rinsed with ultrapure water and subsequently sonicated in ultrapure water for 5 min. Then, it was blown with a gentle N_2 flow and left at room temperature for 30 min before use.

The catalyst ink was prepared by dispersing 5 mg of catalyst in a mixture of 480 μL ultrapure water, 480 μL ethanol, and 40 μL of Nafion aqueous solution followed by sonication for 40 min to form a 5 mg mL^{-1} suspension. A 10- μL portion of the well-dispersed suspension was carefully dropped on a glassy carbon disk electrode (disk diameter: 4 mm, $A_{\text{disk}} = 0.126 \text{ cm}^2$) surrounded by a Pt ring (inner/outer-ring diameter: 5.0/7.0 mm, $A_{\text{ring}} = 0.188 \text{ cm}^2$) with a Teflon separator (rotating ring-disk electrode, RRDE, ALS Co.), yielding a catalyst loading of 0.4 $\text{mg}_{\text{cat}} \text{ cm}^{-2}$. This catalyst loading was selected based on a barely acceptable quality of the catalyst layer. The Nafion content in the catalyst layer was estimated to be about 28 wt%. The catalyst-modified electrodes were dried naturally under ambient conditions for 3 h prior to the electrochemical measurements. For comparison, suspension of 20% Pt/C was also prepared and dropped on a glassy carbon disk of RRDE as a reference using the same procedure as described above, yielding a catalyst loading of 40 $\mu\text{g}_{\text{Pt}} \text{ cm}^{-2}$ (Nafion content: 56 wt%)

The electrochemical measurements, including cyclic voltammetry (CV), linear sweep voltammetry (LSV), and current–time chronoamperometry were conducted on a CHI 832A electrochemical workstation (CH Instruments Inc.) equipped with an RRDE-3A rotating ring disk electrode apparatus (ALS Co.). A Pt coil (ALS, Co.) and Ag/AgCl electrode filled with a saturated KCl aqueous solution (ALS, Co.) were used as the counter and reference electrodes, respectively. All electrochemical measurements were performed in 0.1 M KOH solution at room temperature. High-purity N_2 or O_2 gas was purged into 0.1 M KOH solution with a constant flow rate of 50 mL min^{-1} for at least 30 min to obtain the N_2 - or O_2 -saturated solution prior to the measurement. To correct the background current, the polarization curves measured from LSV in O_2 -saturated 0.1 M KOH was subtracted by those recorded in N_2 -saturated electrolyte.

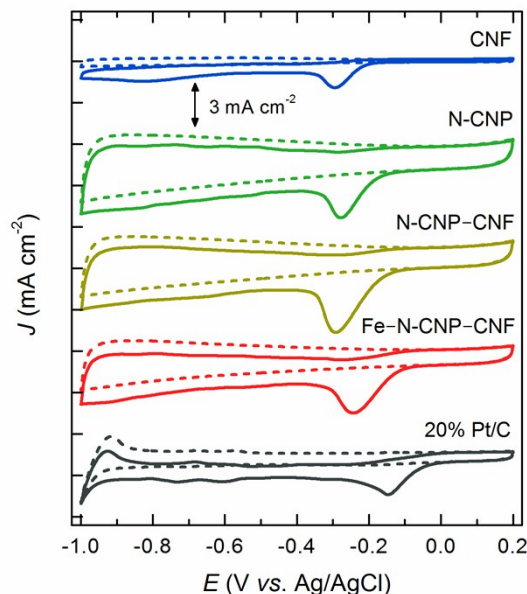


Fig. S13 CV curves of CNF, N-CNP, N-CNP–CNF, Fe–N-CNP–CNF, and 20% Pt/C in N_2 - and O_2 -saturated 0.1 M KOH solution at a scan rate of 50 mV s^{-1} (N_2 : dashed line, O_2 : solid line). Note that the CV curves were recorded after scanning for 20 cycles until the reproducible and stable curves were obtained.

Koutecký–Levich analysis

Rotating ring disk (RDE) measurement was performed to verify the ORR pathway evaluated from the RRDE measurement. A series of polarization curves was recorded at various rotation speeds (*i.e.*, 225, 400, 625, 900, 1225, 1600, 2025, and 2500 rpm) (Fig. S14). It is obvious that the current density in the diffusion-controlled region increases with an increase in rotation speed, which can be explained by faster oxygen diffusion through the electrode surface. On the basis of the polarization curves recorded at various rotation speeds, the electron transfer number (n) per O_2 molecule involved in the ORR process can be determined by the Koutecký–Levich (K–L) equation given as below:⁵⁶

$$\frac{1}{J} = \frac{1}{J_K} + \frac{1}{J_L} = \frac{1}{J_K} + \frac{1}{B\omega^{1/2}}, \quad (\text{S-1})$$

$$B = 0.62nF\nu^{-1/6}C_{O_2}D_{O_2}^{2/3}, \quad (\text{S-2})$$

where J is the measured current density, J_K is the kinetic-limiting current density, J_L is the diffusion-limiting current density, ω is the angular velocity of the disk in rad s^{-1} ($\omega = 2\pi N/60$, N = the RDE rotation rate in rpm), F is the Faraday constant (96485 C mol^{-1}), D_{O_2} is the diffusion coefficient of O_2 in the electrolyte ($1.90 \times 10^{-5} \text{ cm}^2 \text{ s}^{-1}$), ν is the kinematic viscosity of the electrolyte ($0.01 \text{ cm}^2 \text{ s}^{-1}$), and C_{O_2} is the bulk concentration of O_2 in the electrolyte ($1.20 \times 10^{-6} \text{ mol cm}^{-3}$).

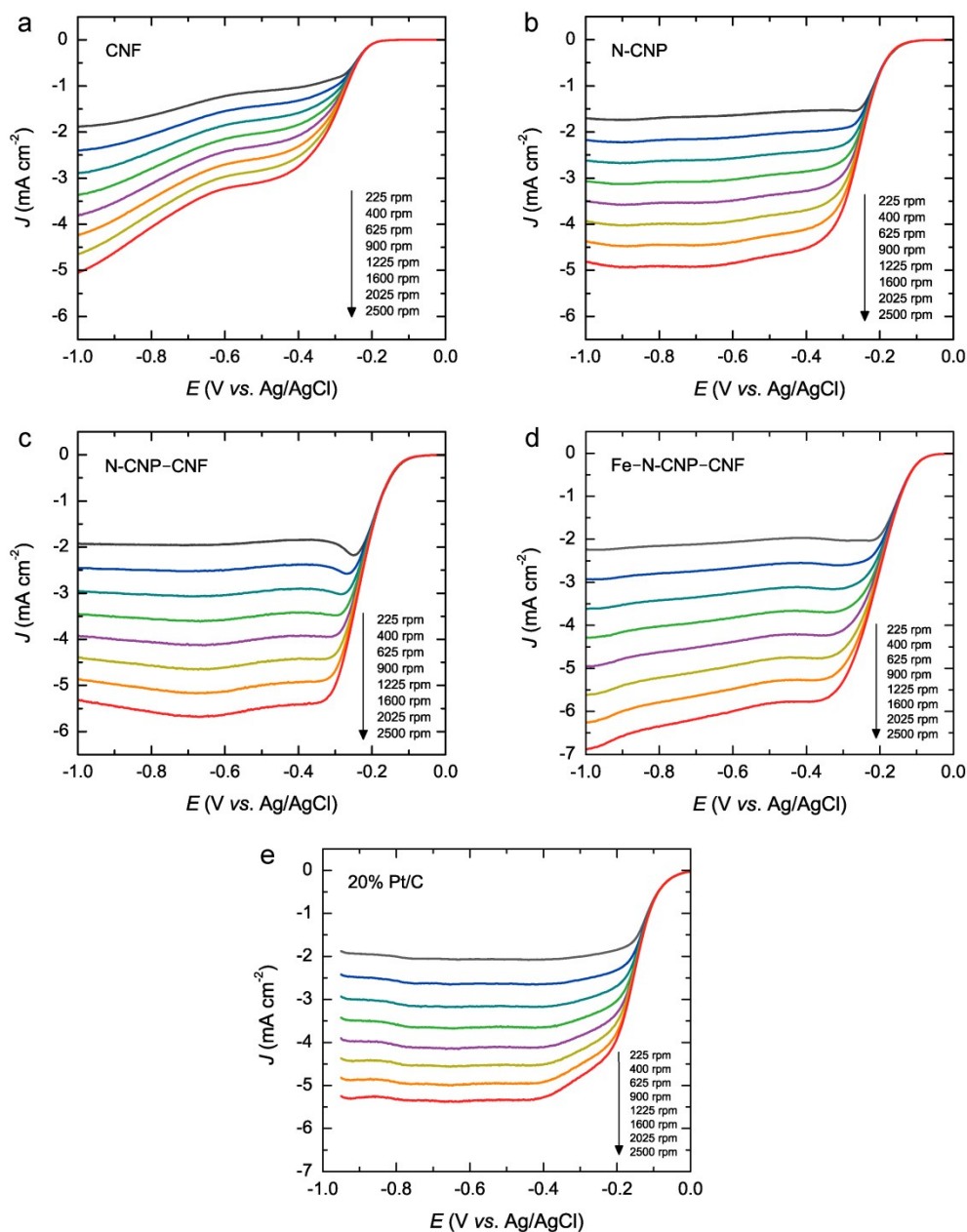


Fig. S14 A series of polarization curves obtained from LSV measurements at various rotation speeds from 225 to 2500 rpm for (a) CNF, (b) N-CNP, (c) N-CNP–CNF, (d) Fe–N-CNP–CNF, and (e) 20% Pt/C in O₂-saturated 0.1 M KOH solution (after background current correction).

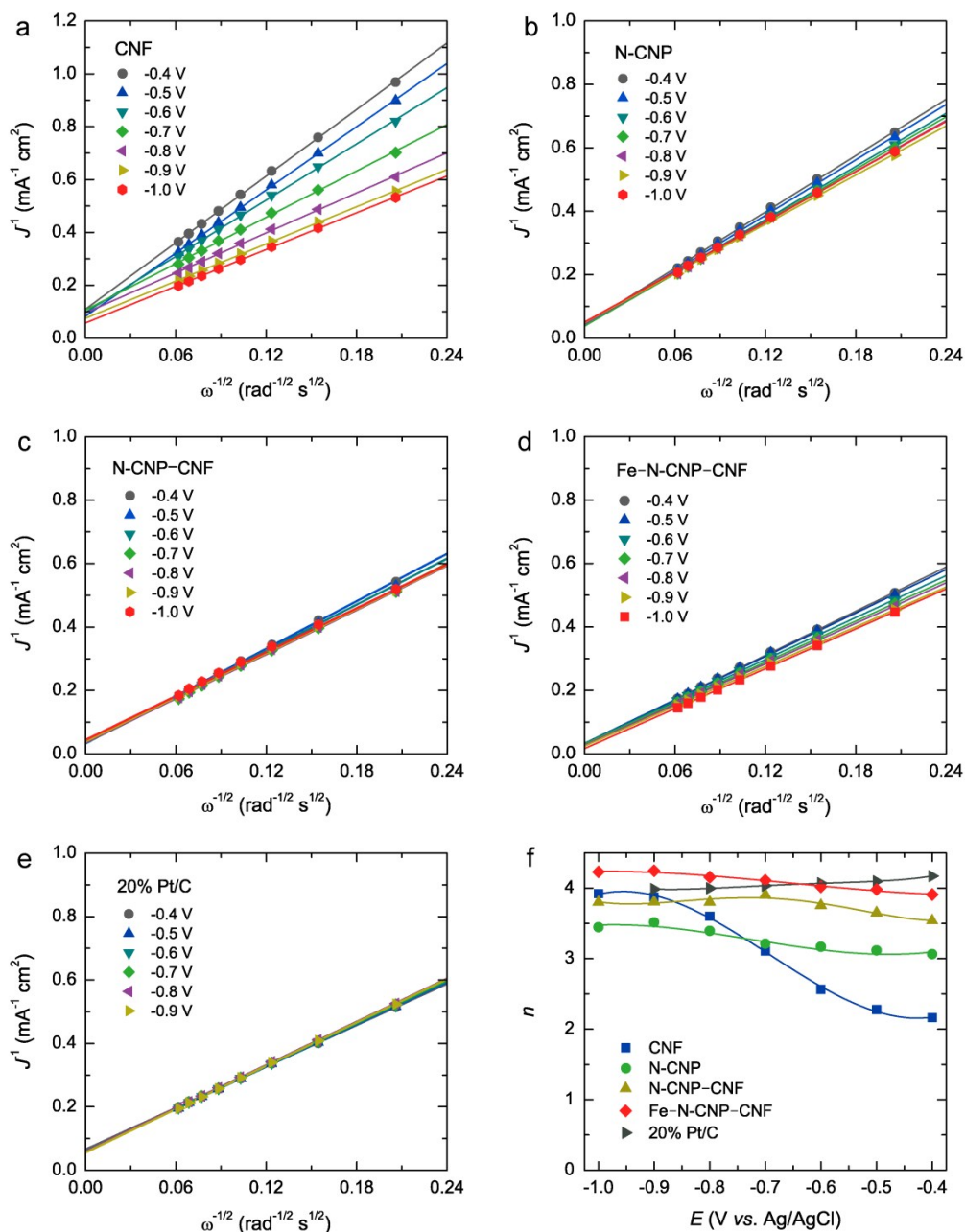


Fig. S15 The K–L plots of (a) CNF, (b) N-CNP, (c) N-CNP–CNF, (d) Fe–N-CNP–CNF, and (e) 20% Pt/C in the potential range from -1.0 to -0.4 V derived from a series of polarization curves at various rotation speeds in Fig. S14. (f) Electron transfer numbers (n) calculated from the slopes of linear fit lines of all catalysts in the potential range from -1.0 to -0.4 V.

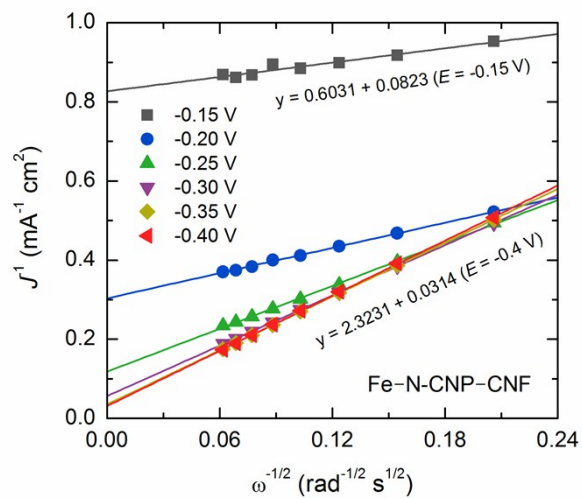


Fig. S16 The K–L plots of Fe–N–CNP–CNF in the kinetic controlled region.

Table S4 Comparison of ORR performances of Fe–N-doped carbons in recent literature

Catalyst	E (V vs. RHE) ^a		n / E (V vs. RHE) ^a		Catalyst loading (mg cm ⁻²)	Nafion content (% by weight) ^b	Ref.
	E_{onset}	$E_{1/2}$	K-L plot	RRDE			
Fe-N _{70%} /C-800	0.91	0.75	3.7-3.9 / 0.3–0.7 V	-	0.27	50	[S7]
Fe-N-graphene	1.01	0.8	-	3.99	0.40	5	[S8]
CPL-Fe	0.89	0.74	3.7 / 0.55–0.7 V	-	0.30	-	[S9]
Fe/N/C	0.93	0.84	3.96 / 0.5 V	-	0.46	29	[S10]
Fe-N doped CNT/graphene	0.92	0.84	4 / 0.6–0.8 V	3.99–4.0 / 0.2–0.8 V	0.60	17	[S11]
NG/Fe _{10.0} -900	0.91	0.75	4.1 / 0.5 V	-	0.05	83	[S12]
Fe-N-C700	0.87	0.79	4.1 / (0.17–0.67 V)	-	0.06	57	[S13]
Fe@C-FeNC-2	0.98	0.90	-	3.95–3.99 / 0.4–0.8 V	0.70	-	[S14]
Fe-N/C-800	0.923	0.809	4.15	3.96 / 0.1–1.1 V	0.10	-	[S15]
Fe/Fe ₃ C@N-C	0.911	0.779	-	3.9 / 0.2–0.8 V	0.60	0.5	[S16]
N-Fe-nC	0.92	0.84	-	3.88–3.98 / 0.17–0.77	0.36	20	[S17]
CNT@Fe-N-C-700	0.90	0.80	-	3.95-4.0 / 0.4–0.8 V	0.38	33	[S18]
PANI-4.5Fe-HT2 (SBA15)	0.95	0.84	3.4–4.0 / 0.42–0.77 V	-	0.08	-	[S19]
FePc-Py-CNTs	0.97	0.915	-	4 / 0.4–0.8 V	0.32	56	[S20]
Fe-CN-20-1000	1.04	0.88	-	3.99 / 0.2–0.8 V	0.75	-	[S21]
Fe ₃ C@NCNF-900	0.98	0.89	3.8 / 0.5 V	-	0.15	0.4	[S22]
Fe ₃ C/NCNT	0.95	0.86	4.2 / 0.2–0.6 V	4	0.40	33	[S23]
NGFe-800	0.82	0.73	3.95 / 0.6 V	-	0.30	33	[S24]

Catalyst	E (V vs. RHE) ^a		n / E (V vs. RHE) ^a		Catalyst loading (mg cm ⁻²)	Nafion content (% by weight) ^b	Ref.
	E_{onset}	$E_{1/2}$	K-L plot	RRDE			
FeNC-800	1.1	0.88	-	3.99 / 0.2–0.9 V	0.90	-	[S25]
Fe/NC800	0.95	0.84	-	3.9–4.0 / 0.2–0.8 V	0.40	-	[S26]
Fe/N-CNT	0.96	0.81	3.85 / 0.3–0.7 V	-	0.19	39	[S27]
Fe-N-CNF	0.95	0.83	3.93–3.95 / 0.4–0.6 V	-	0.60	5	[S28]
Fe ₃ N-OMC	0.99	0.84	-	3.9 / 0–0.9 V	0.08	33	[S29]
Fe ₃ -NG	1.025	0.837	-	3.78–3.97 / 0.1–0.8 V	0.50	63	[S30]
PMF	0.97	0.86	-	3.99	1.20	37	[S31]
Fe-N-CNT-OPC	0.92	0.83	-	3.90–3.99 / 0.4–0.8 V	0.08	-	[S32]
Fe-N/C-700	0.956	0.840	4.02 / 0.35–0.75 V	-	0.15	20	[S33]
Fe-N-CNP-CNF	0.87	0.78	3.9–4.1 / 0.4–0.7 V	3.61–3.88 / 0.4–0.9 V	0.40	28	This work

a) The measured potentials vs. Ag/AgCl were converted to the reversible hydrogen electrode (RHE) scale according to the Nernst equation:

$$E_{RHE} = E_{Ag/AgCl} + 0.591pH + E_{Ag/AgCl}^0 \quad (S-3)$$

where E_{RHE} is the converted potential vs. RHE, $E_{Ag/AgCl}^0 = 0.1976$ at 25°C, and $E_{Ag/AgCl}$ is the experimentally measured potential against Ag/AgCl reference.

b) The Nafion content in the catalyst layer was determined as the percentage of Nafion and total catalyst weight using the following relation:^[S34]

$$\text{Nafion content (\%)} = \frac{\text{Nafion loading (mg cm}^{-2}\text{)}}{\text{Nafion loading (mg cm}^{-2}\text{)} + \text{Catalyst loading (mg cm}^{-2}\text{)}} \times 100 \quad (S-4)$$

References

- [S1] M. Endo, Y. A. Kim, T. Hayashi, Y. Fukai, K. Oshida, M. Terrones, T. Yanagisawa, S. Higaki and M. S. Dresselhaus, *Appl. Phys. Lett.*, 2002, **80**, 1267.
- [S2] S. S. Harilal, R. C. Issac, C. V. Bindhy, V. P. N. Nampoore and C. P. G. Vallaban, *J. Phys. D: Appl. Phys.*, 1995, **30**, 1703.
- [S3] E. Tatarova, F. M. Dias and C. M. Ferreira, *Int. J. Hydrogen Energy*, 2009, **34**, 9585.
- [S4] A. E. Lefohn, N. M. Mackie and E. R. Fisher, *Plasmas Polym.*, 1998, **3**, 197.
- [S5] J. M. Stillahn and E. R. Fisher, *J. Phys. Chem. A*, 2010, **114**, 5287.
- [S6] S. Ye and A. K. Vijh, *J. Solid State Electrochem.*, 2005, **9**, 146.
- [S7] Q. Cui, S. Chao, P. Wang, Z. Bai, H. Yan, K. Wang and L. Yang, *RSC Adv.*, 2014, **4**, 12168.
- [S8] C. He, J. J. Zhang and P. K. Shen, *J. Mater. Chem. A*, 2014, **2**, 3231.
- [S9] J. Zhang, S. Wu, X. Chen, K. Cheng, M. Pan and S. Mu, *RSC Adv.*, 2014, **4**, 32811.
- [S10] J. Du, F. Cheng, S. Wang, T. Zhang and J. Chen, *Sci. Rep.*, 2014, **4**, 4386.
- [S11] S. Zhang, H. Zhang, Q. Liu and S. Chen, *J. Mater. Chem. A*, 2013, **1**, 3302.
- [S12] K. Pavez, S. Yang, Y. Hernandez, A. Winter, A. Turchanin, X. Feng and K. Müllen, *ACS Nano*, 2012, **6**, 9541.
- [S13] A. Kong, B. Dong, X. Zhu, Y. Kong, J. Zhang and Y. Shan, *Chem. Eur. J.*, 2013, **19**, 16170.
- [S14] W.-J. Jiang, L. Gu, L. Li, X. Zhang, L.-J. Zhang, J.-Q. Wang, J.-S. Hu, Z. Wei and L.-J. Wan, *J. Am. Chem. Soc.*, 2016, **138**, 3570.
- [S15] L. Lin, Q. Zhu and A.-W. Xu, *J. Am. Chem. Soc.*, 2014, **136**, 11027.
- [S16] Y. Zhang, L.-B. Huang, W.-J. Jiang, X. Zhang, Y.-Y. Chen, Z. Wei, L.-J. Wan and J.-S. Hu, *J. Mater. Chem. A*, 2016, **4**, 7781.
- [S17] X. Wang, H. Fe, W. Li, J. Zheng and X. Li, *RSC Adv.*, 2014, **4**, 37779.
- [S18] Y. Yao, H. Xiao, P. Wang, P. Su, Z. Shao and Q. Yang, *J. Mater. Chem. A*, 2014, **2**, 11768.
- [S19] X-H. Yan and B.-Q. Xu, *J. Mater. Chem. A*, 2014, **2**, 8617.
- [S20] R. Cao, R. Thapa, H. Kim, X. Xu, M. G. Kim, Q. Li, N. Park, M. Liu and J. Cho, *Nat. Commun.*, 2013, **4**, 2076.
- [S21] T. Liu, P. Zhao, X. Hua, W. Luo, S. Chen and G. Cheng, *J. Mater. Chem. A*, 2016, **40**, 11357.
- [S22] G. Ren, X. Lu, Y. Li, Y. Zhu, L. Dai and L. Jiang, *ACS Appl. Mater. Interfaces*, 2016, **8**, 4118.
- [S23] J. Zhu, M. Xiao, C. Liu, J. Ge, J. St-Pierre and W. Xing, *J. Mater. Chem. A*, 2015, **3**, 21451.
- [S24] H. Feng, L. Wang, L. Zhao, C. Tian, P. Yu and H. Yu, *Phys. Chem. Chem. Phys.*, 2016, **18**, 26572.
- [S25] P. Zhao, W. Xu, X. Hua, W. Luo, S. Chen and G. Cheng, *J. Phys. Chem. C*, 2016, **120**, 11066.
- [S26] Y. Qian, J. Cavanaugh, I. A. Khan, X. Wang, Y. Peng, Z. Hu, Y. Wang and D. Zhao, *ChemPlusChem*, 2016, **81**, 718.
- [S27] Y. Liu, H. Jiang, Y. Zhu, X. Yang and C. Li, *J. Mater. Chem. A*, 2016, **4**, 1694-1701.
- [S28] Z.-Y. Wu, X.-X. Xu, B.-C. Hu, H.-W. Liang, Y. Lin, L.-F. Chen and S.-H. Yu, *Angew. Chem. Int. Ed.*, 2015, **54**, 8179.
- [S29] X. Liu, S. Zou and S. Chen, *Nanoscale*, 2016, **8**, 19249.

- [S30] X. Cui, S. Yang, X. Yan, J. Leng, S. Shunag, P. M. Ajayan and Z. Zhang, *Adv. Func. Mater.*, 2016, **26**, 5708.
- [S31] W. Yang, X. Liu, X. Yue, J. Jia and S. Guo, *J. Am. Chem. Soc.*, 2015, **137**, 1436.
- [S32] J. Liang, R. F. Zhou, X. M. Chen, Y. H. Tang and S. Z. Qiao, *Adv. Mater.*, 2014, **26**, 6074.
- [S33] Z. K. Yang, L. Lin and A.-W. Xu, *Small*, 2016, **12**, 5710.
- [S34] E. Passalacqua, F. Lufrano, G. Squadrito, A. Patti and L. Giorgi, *Electrochim. Acta*, 2001, **46**, 799.